Article:

Brisset, Alexandra Helene Marie Brigitte orcid.org/0000-0003-3217-1106, Bieniek, M, Invernizzi, Laurent et al. (3 more authors) (2023) The formation of O and H radicals in a pulsed discharge in atmospheric pressure helium with water vapour admixtures. Plasma Sources Science and Technology. 065004. ISSN 0963-0252

https://doi.org/10.1088/1361-6595/acd57f

Plasma Sources Science and Technology

PAPER • OPEN ACCESS

The formation of O and H radicals in a pulsed discharge in atmospheric pressure helium with water vapour admixtures

To cite this article: Alexandra Brisset *et al* 2023 *Plasma Sources Sci. Technol.* **32** 065004

OPEN ACCESS
IOP Publishing
Plasma Sources Science and Technology
Plasma Sources Sci. Technol. **32** (2023) 065004 (17pp)
https://doi.org/10.1088/1361-6595/acd57f

The formation of O and H radicals in a pulsed discharge in atmospheric pressure helium with water vapour admixtures

Alexandra Brisset[1], Matthew Bieniek[2], Laurent Invernizzi[1], Mohammad Hasan[2], James Walsh[2], Kari Niemi[1] and Erik Wagenaars[1,*]

[1] York Plasma Institute, Department of Physics, University of York, York YO10 5DD, United Kingdom
[2] Department of Electrical Engineering and Electronics, University of Liverpool, Liverpool, Merseyside, United Kingdom

E-mail: erik.wagenaars@york.ac.uk

Received 6 October 2022, revised 19 April 2023
Accepted for publication 15 May 2023
Published 6 June 2023

Abstract

The spatio-temporal distribution of O and H radicals in a 90 ns pulsed discharge, generated in a pin–pin geometry with a 2.2 mm gap, in He + H_2O (0.1% and 0.25%), is studied both experimentally and by 1D fluid modelling. The density of O and H radicals as well as the effective lifetimes of their excited states are measured using picosecond resolution two-photon absorption laser induced fluorescence. Good agreement between experiments and modelling is obtained for the species densities. The density of O and H is found to be homogenous along the discharge axis. Even though the high voltage pulse is 90 ns long, the density of O peaks only about 1 μs after the end of the current pulse, reaching 2×10^{16} cm^{-3} at 0.1% H_2O. It then remains nearly constant over 10 μs before decaying. Modelling indicates that the electron temperature (Te) in the centre of the vessel geometry ranges from 6 to 4 eV during the peak of discharge current, and after 90 ns, drops below 0.5 eV in about 50 ns. Consequently, during the discharge (<100 ns), O is predominantly produced by direct dissociation of O_2 by electron impact, and in the early afterglow (from 100 ns to 1 μs) O is produced by dissociative recombination of O_2^+. The main loss mechanism of O is initially electron impact ionisation and once T_e has dropped, it becomes mainly Penning ionisation with $He_2{}^*$ and He^* as well as three-body recombination with O^+ and He. On time scales of 100–200 μs, O is mainly lost by radial diffusion. The production of H shows a similar behaviour, reaching 0.45×10^{16} cm^{-3} at 1 μs, due to direct dissociation of H_2O by electron impact (<100 ns) followed by electron–ion recombination processes (from 200 ns to 1.5 us). H is dominantly lost through Penning ionisation with He^* and $He_2{}^*$ and by electron impact ionisation, and by charge exchange with O^+. Increasing concentrations of water vapour, from 0.1% to 0.25%, have little effect on the nature of the processes of H formation but trigger a stronger initial production of O, which is not currently reproduced satisfactorily by the modelling. What emerges from this study is that the

---

[*] Author to whom any correspondence should be addressed.

built up of O and H densities in pulsed discharges continues after electron-impact dissociation processes with additional afterglow processes, not least through the dissociative recombination of O_2^+ and H_2^+.

Keywords: two-photon absorption laser induced fluorescence, nanosecond discharge, radical density/distribution, 1D fluid modelling

(Some figures may appear in colour only in the online journal)

1. Introduction

Pulsed non-thermal atmospheric pressure plasmas (NT-APPs) combine valuable features for industrial applications in fields as varied as surface processing, assisted combustion, or plasma medicine [1–5]. They have proven that they could be very stable even at atmospheric pressure and can even cover large diffuse volumes of activated gas when a very strong overvoltage is applied (voltage above breakdown voltage) [6–10]. More commonly, pulsed discharges can greatly improve the energy efficiency of the production of reactive species compared to the use of continuous or AC discharges [11]. The plasma chemistry and the pathways of production of the key reactive species can vary critically depending on the plasma parameters. Detailed knowledge of the plasma chemistry is usually required to control and optimise the use of plasma sources for applications. O and H are highly reactive and are key precursors of long-living species such as NO_x, O_3 and H_2O_2. Their quantification is therefore necessary to unravel the chemical pathways in pulsed APPs.

Pulsed APPs can be run both in noble gases (He, Ar, Xe, … with or without admixtures or molecular gases) and in molecular gases (air, air and combustible admixtures (methane/ethane, …), CO_2, …) [12–16]. For biomedical purposes, discharges generated in Helium and Argon can be easily maintained at room temperature (in particular He) and ignited at lower voltages than for other feed gases. With an addition of up to a few percent of molecular species in the feed gas or by mixing with ambient air, NT-APPs produce significant concentrations of reactive oxygen and nitrogen species (RONS). Numerous studies were undertaken to unravel the very complex chemistry of APPs in He with molecular species admixing and ambient air mixing [17–26]. To efficiently produce oxygen containing species (e.g. O, $O(^1D)$, $O(^1S)$, $O_2(v)$, $O_2(a)$, $O_2(b)$, O_3, …), molecular oxygen or air is often added to the feed gas. Other works focused on admixing water vapour which is quasi ubiquitous in plasma medicine and leads to the production of some of the most reactive species (OH, H_2O_2, HO_2, …). Despite the additional complexity of the chemistry, numerical studies gave a hint of the evolution of major reactive species in mixtures of He + O_2 + H_2O [13, 17, 27]. In [28], the ground state O density experimentally measured in the channel of a RF COST-like jet run in He + H_2O was two orders of magnitude lower than that measured in a related configuration in He + O_2 [19] or in a cylindrical RF plasma jet in He + O_2 in [29]. This is because the production of O from O_2 is more efficient than from H_2O in these discharges. In regard with this difference in production efficiency, the work of [28] also highlighted that the common presence of impurities such as O_2 [20, 28], can play a significant or even dominant role in the production of O compared to the molecular species intentionally introduced like H_2O, when the later are introduced in low concentrations. In the effluent of APPJs, various processes can take place that consume or generate RONS downstream and even in the far effluent. In [30, 31], VUV radiation was detected far in the effluent region of two He + O_2 APPJs in a helium controlled atmosphere and is believed to maintain a relatively high O density in the far effluent ($\sim$1014 cm^{-3}). In the channel, O is mainly produced by electron impact reactions and lost by heavy species particle recombination [31]. When water vapour is introduced, H-based reactive species are also produced. OH kinetics in He + H_2O pin–pin pulsed discharges was studied by Verreycken *et al* in both a low electron density mode, as in this work, and a high density mode, for which the strong ionisation leads to important charge exchange and dissociative recombination processes in the highly ionised plasma core [32]. In He + H_2O, the role of secondary species such as HO_2 has also been studied in capacitively coupled discharges and plasma jets [19, 33]. In particular, HO_2 plays a role in the acidification of plasma treated liquids due to the low dissolution reaction of HO_2 in water ($HO_2 \rightarrow H^+ + O_2^-$). Its production is fostered by the presence of O_2 through: $He + H + O_2 \rightarrow He + HO_2$. With increasing water vapour concentration, the impact on the production of reactive species is manifold since it also affects the electron properties and discharge development with competing effects. In the pin–pin negative pulse discharge studied in [34], it was observed that the discharge propagation is slower than in dry conditions probably due to a lower initial electron density left by the previous pulse, but the channel conductivity becomes higher at the instant of breakdown due to higher ionisation rates of water than He, leading to a faster return wave in the presence of water vapour and consequently leading to a faster current rise. The effect on electron properties also significantly affects reaction rates. In RF He + H_2O discharges at atmospheric pressure, the electron density lowers with increasing water concentration, while the mean electron temperature increases, leading to complex behaviours of reactions by electronic impact with increasing water concentration (e.g. OH production by electron impact dissociation of water [18]). Consequently, the rise of the species density with increasing water vapour can be nonlinear. In [34], the electron density was shown to drop by a factor about 2 with the introduction of 0.25% H_2O to a He feed gas and the electron recombination was much faster due to dissociative recombination with ions and water clusters (O_2^+, $H_2O_3{}^+$, etc). In [35], a nanosecond pulsed diffuse discharge is generated over liquid water in He with or without O_2. n_e and T_e were measured by incoherent Thomson scattering. The maximum electron density reached $\sim 5 \times 10^{14}$ cm^{-3} during the pulse. The electron temperature measured soon after at the beginning of the pulse was about 4 eV and dropped quickly with voltage down to less than 0.5 eV at the end of the pulse. In general, in streamer discharges, the mean electron temperature in the streamer head is about 4–10 eV [32, 36, 37], while the electron temperature during the conduction phase is down to 1–2 eV at most. At such electron densities and temperatures, in He + H_2O, it is expected that electron impact reactions dominate the production of ROS during the discharge and that recombination processes dominate in the early and late afterglow as will be demonstrated in this paper through comparison of experimental and numerical simulation.

The general objectives of this work are to study the kinetics of reactive species, in particular O and H, in a fast pulsed discharge (rise rate $\sim$80 V ns^{-1}) generated at atmospheric pressure in an enclosed chamber wherein pure or humid Helium (up to 0.25% H_2O) is present. Densities of O and H are obtained experimentally by picosecond resolution two-photon absorption laser induced fluorescence (ps-TALIF) and are combined with 1D fluid modelling to investigate the reaction mechanisms for O and H production.

The measurement of the spatio-temporal evolution of atomic species in non-homogenous atmospheric plasmas requires spectroscopic or laser methods. TALIF is based on the measurement of the fluorescence emitted by a laser pulse excited state of the probed atomic species. The density of the atomic species in its ground state is related to the fluorescence signal through a system of rate equations that depend on the population/depopulation mechanisms of these states. This system of equations is valid under certain excitation conditions that will be discussed in this paper. Under these conditions, TALIF requires the precise knowledge of the fluorescence decay times but at atmospheric pressure, quenching is strong and these decay times are of the order of a few nanoseconds or less, while the quenching partners are largely unknown. Thus, quenching cannot be accurately calculated and the use of fs or ps laser pulses and detection systems are necessary to determine the decay time accurately. In this work, TALIF is performed in the unsaturated regime with a ps pulse to resolve the fluorescence decay times. Oxygen calibration is performed with a xenon source and hydrogen with a krypton source. This method has already been described in a number of sources [29, 38–44].

One-dimensional plasma fluid modelling was performed to better understand the reaction kinetics of O and H as measured in the experiments. The model and chemistry set used are described and discussed in section 3 and in the appendix respectively.

2. Experimental setup and method

2.1. The discharge system

The discharge is generated in a 2.2 mm gap pin-to-pin electrode geometry enclosed in a 0.3 l vessel. The electrodes are both made of stainless steel, they are symmetric of conical shape with a tip which radius of curvature is around 500 μm. A positive high-voltage nanosecond pulse is applied to one of the pins by means of a high voltage DC supply coupled to a home-made switch box delivering a pulse of about 2 kV voltage, 35 ns rise time (10%–90%) and 90 ns duration FWHM at 0.1% H_2O (80 ns at 0.25% H_2O), see figure 1. The energy dissipated in the discharge is kept constant at 90 μJ by adjusting the voltage amplitude. The discharge is run at 5 kHz. The voltage is measured using a high bandwidth probe (Tektronix P5100A 500 MHz) and the current with a Rogowski coil probe—CM-100-L, 1.0 V A^{-1} (Ion Physics). The applied voltage and the discharge current are recorded with a 1 GHz–10 Gs s^{-1} digital oscilloscope (LeCroy wavesurfer 10). The discharge is generated in helium (99.996% purity) with a total controlled flow rate of 1 l min^{-1}, injected in the vessel sideways to the axis of the electrodes (about 3 cm from the discharge axis). Water vapour is admixed to the gas flow by guiding a fraction of the total helium flow through a glass bubbler filled with distilled water as in [18]. The amount of water vapour is calculated using the vapour pressure at room temperature and the flow rate through the bubbler. Most of the lines are made of stainless steel to limit the level of impurities in the gas. The output gas of the reactor is guided to an exhaust several metres downstream.

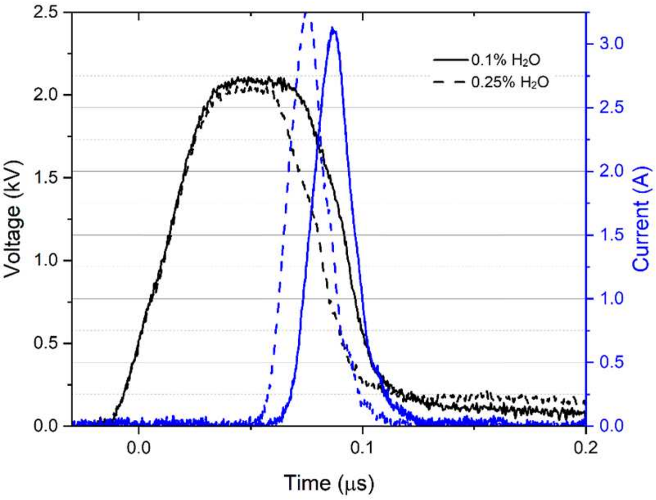

Figure 1. Typical voltage and current signals in He + 0.1% and 0.25% H_2O for a gap of 2.2 mm.

2.2. The laser and fluorescence detection setup

The laser and detection setup are illustrated in figure 2. An Nd:YAG pumped picosecond laser at 1064 nm is coupled first to an amplifier (APL2100, Ekspla) and second to a system (PG411, Ekspla) made of (i) a parametric generator (OPO + OPA), (ii) a second harmonic generator (FSH/SSH) and (iii) a deep UV extension system. It enables to generate a 30 ps-laser pulse of up to a few hundreds of μJ that can be tuned in the range 193–2300 nm with a spectral bandwidth of about 4 cm^{-1}, at 10 Hz.

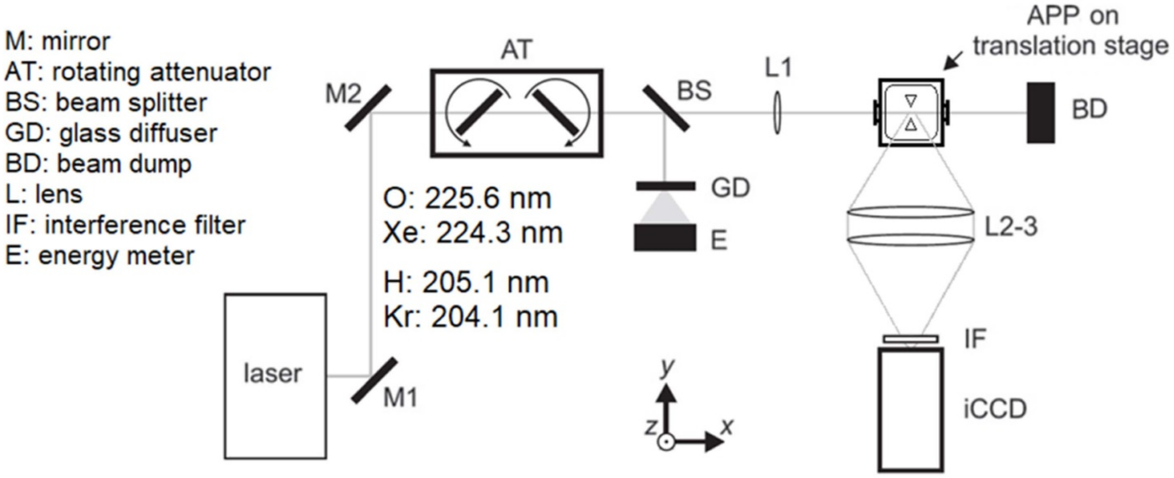

Figure 2. Laser and fluorescence detection setup adapted from [28]. Reproduced from [28]. © The Author(s). Published by IOP Publishing Ltd CC BY 4.0.

The laser pulse energy is controlled over time with a pair of rotating attenuators coupled to an energy meter. At every laser shot, the energy is monitored and compared to the target energy value and the pair of attenuators is rotated accordingly by a stepper motor to increase or lower the laser beam energy of the next shot. A pair of attenuators is used to compensate for the laser beam deviation across each attenuator and keep a straight laser beam line. The attenuators are coated CaF_2 substrates (Layertec®). The standard deviation of the shot-to-shot fluctuations in the pulse energy is about 6%.

The laser beam is focused with a 30 cm focal length lens into the discharge gap plane, the focus point being a few centimetres after the discharge axis to get a laser beam diameter of 300 μm at the point of TALIF measurement, between the electrodes. The laser beam diameter is measured by sliding a razor blade across the laser beam while its energy is recorded. This beam diameter was chosen to get sufficient TALIF signal and spatial resolution while avoiding saturation of the two-photon transition or laser-plasma interactions (photo-ionisation and photo-dissociation, here) and to avoid any damage of the reactor windows and cuvette walls. The laser beam is then stopped by a beam dump.

The fluorescence emission of the laser pulse excited state is collected at 90° by a doublet of achromatic lenses (diameter 50 mm each, effective focal length 80 mm) and recorded with a 4Picos ICCD camera from Stanford Computer Optics (780 × 580 array, 8.3 μm^2 pixels, S25IR photocathode) equipped with an interference filter placed in front of the camera (central wavelengths $\lambda_O = 844.5 \pm 0.5$ nm, $\lambda_H = 656$ nm ± 5 nm, $\lambda_{Xe} = 835 \pm 5$ nm, $\lambda_{Kr} = 825 \pm 5$ nm) to eliminate stray light and fluorescence at other wavelengths. To increase the signal to noise ratio, the fluorescence signal of 30–300 shots has been accumulated on the ICCD. The camera is triggered by a TTL output signal from the laser which has only 5 ps jitter with the laser pulse, and the internal camera jitter between the gate opening and the reception of the trigger signal is only 10 ps, allowing the measurement of sub-nanosecond fluorescence lifetimes (see table 1).

The TALIF technique is performed in the non-saturated regime using the noble-gas calibration technique [38–44].

In this regime, the density n_x of the ground state species x is related to the density of the gas used for calibration n_{cal} through:

$$\frac{S_{\mathrm{F},x}}{S_{\mathrm{F,cal}}} = \frac{\eta\left(\lambda_{\mathrm{F},x}\right)}{\eta\left(\lambda_{\mathrm{F,cal}}\right)} \frac{T_{\mathrm{f}}\left(\lambda_{\mathrm{F},x}\right)}{T_{\mathrm{f}}\left(\lambda_{\mathrm{F,cal}}\right)} \frac{T_{\mathrm{w}}\left(\lambda_{\mathrm{F},x}\right)}{T_{\mathrm{c}}\left(\lambda_{\mathrm{F,cal}}\right)} \frac{a_{ik,x}}{a_{ik,\mathrm{cal}}} \frac{\sigma_x^{(2)}}{\sigma_{\mathrm{cal}}^{(2)}} \frac{n_x}{n_{\mathrm{cal}}} \times \left(\frac{E_{\mathrm{L},x}}{E_{\mathrm{L,cal}}} \frac{\lambda_{\mathrm{L},x}}{\lambda_{\mathrm{L,cal}}}\right)^2$$

where S_{F} is the measured fluorescence signal that has been integrated spatially, temporally and spectrally, $\eta\left(\lambda_{\mathrm{F}}\right)$ is the camera quantum efficiency at the fluorescence wavelength λ_{F}, $T_{\mathrm{f/w/c}}$ are the transmission coefficients of the filter/reactor window/cuvette wall, a_{ik} are the branching ratios of the transitions ($a_{ik} = \frac{A_{ik}}{\sum_k A_{ik} + \sum_q k_q^i n_q}$, where A_{ik} is the Einstein coefficient of the transition from state i to k, $k_q^i n_q$ is the quenching rate between state i and q), $\sigma^{(2)}$ are the cross sections for two-photon absorption, E is the laser energy at the position of TALIF measurement and $\lambda_{\mathrm{L}is}$ the laser wavelength.

The atomic species probed are oxygen and hydrogen and the associated calibration gases used for TALIF analysis are respectively xenon and krypton. The TALIF schemes for these species are as illustrated in figure 3 of [28]. The ground state of atomic oxygen $\mathrm{O(2p^4\,{}^3P}_J)$, as well as the excited states $\mathrm{O(3p\,{}^3P}_J)$, are triplet states with $J = 0,1,2$. The laser wavelength for two-photon absorption of this transition from $J = 2$ is 225.6 nm. Relaxation of the triplet upper state happens through quenching and radiative emission at 844.6 nm. To get the total density of the ground triplet state of O, it is necessary to correct the density of the level $J = 2$ measured (n_2) with the Boltzmann factor: $n_O = \frac{n_2}{g_2} \sum_{J=0,1,2} g_J \mathrm{e}^{-E_J/(k_{\mathrm{B}} T_{\mathrm{B}})}$, where the spectral parameters can be found on the NIST database. The gas temperature was estimated from [34]. With a linearly polarised laser at 205.1 nm, the ground state of atomic hydrogen $\mathrm{H(1s\,{}^2S_{1/2})}$ can be excited to the two sub-levels $\mathrm{H(3s\,{}^2S_{1/2})}$

Table 1. Parameters for TALIF analysis.

	Pressure	λ_L (nm)	λ_F (nm)	*ratio of* $\sigma^{(2)}$	A_{ik} (s^{-1})	τ_{ik} (ns)	E_L (μJ)
O	1 atm	225.6	844.6	$\frac{\sigma^{(2)}_{Xe}}{\sum_{J'}\sigma^{(2)}_{O,J\to J'}} = 1.02 \pm 0.2$	2.88×10^7	9 ± 0.5	19.6
Xe	200 Pa	224.3	834.9		3.08×10^7	13	0.64
H	1 atm	205.1	656.3	$\frac{\sigma^{(2)}_{Kr}}{\sigma^{(2)}_{H}} = 0.62 \pm 0.31$	4.41×10^7	1.7 ± 0.1	7.9
Kr	200 Pa	204.1	826.3		2.79×10^7	14	0.55

Reference for $\sigma^{(2)}_{Xe}$ [1]:—reference for $\sigma^{(2)}_{O}$ [2]:—reference for A_{ik} [3]. The uncertainty of the measured fluorescence lifetime of O and H is given by the standard deviation of repeated measurements.

and H(3d $^2D_{3/2,5/2}$) of 0.15 cm^{-1} spectral separation, much lower than the laser spectral width. Relaxation of these three upper states happens mostly through quenching and radiative emission at 656.3 nm with a natural lifetime of the weighted combination of the 3s and 3d sublevels of 17.6 ns [45]. Selection rules prevent the sub-level 3p $^2P_{1/2,3/2}$ to be excited by the laser. However, L-mixing, i.e. the redistribution of the population in the three mentioned higher excited levels of atomic hydrogen, can lead to a loss of fluorescence signal. However, since the work of Preppernau *et al* [46], the significance of that process was not established clearly and the experimental measurement of the lifetime of H ($n = 3$) is used for calibration. The TALIF schemes considered for the rare gases are simpler. The ground state of Xenon Xe($5p^6\,{}^1S_0$) is excited to the single upper state Xe($6p'[3/2]_2$). It relaxes through quenching and radiative emission to several lower states, in particular Xe($6s'[1/2]_1$) at 834.91 nm, with an optical branching ratio of 0.733 [47]. The ground state of Krypton (Kr($4p^6\,{}^1S_0$) is excited to the single upper state Kr($5p'[3/2]_2$), that radiates to the lower state Kr($5s'[1/2]_1$) at 826.32 nm with an optical branching ratio of 0.953 [48].

The parameters used for the TALIF measurement of oxygen, hydrogen, xenon and krypton densities are given in table 1. In particular, it should be noted that the value of the two-photon cross section of Xenon used in this work is the recently measured value given in [49].

3. Modelling and numerics

A one-dimensional plasma fluid model was employed in this work, which is based on a system of differential equations, comprised of the equations of continuity of the flux density of electrons, electron energy, ions, and neutral species, and Poisson's equation (as in e.g. [50–52]):

$$\frac{\partial n_e}{\partial t} + \nabla\cdot\boldsymbol{J}_e = S_e - \frac{\Gamma_e}{R}, \quad \boldsymbol{J}_e = -D_e\nabla n_e + n_e\mu_e\nabla\varphi; \quad (1)$$

$$\frac{\partial n_\varepsilon}{\partial t} + \nabla\cdot\boldsymbol{J}_\varepsilon = e\boldsymbol{J}_e\cdot\nabla\varphi - S_\varepsilon, \quad \boldsymbol{J}_\varepsilon = -D_\varepsilon\nabla n_\varepsilon + n_\varepsilon\mu_\varepsilon\nabla\varphi; \quad (2)$$

$$\frac{\partial n_{ip}}{\partial t} + \nabla\cdot\boldsymbol{J}_{ip} = S_{ip} - \frac{\Gamma_{ip}}{R}, \quad \boldsymbol{J}_{ip} = -D_{ip}\nabla n_{ip} - n_{ip}\mu_{ip}\nabla\varphi; \quad (3)$$

$$\frac{\partial n_{in}}{\partial t} + \nabla\cdot\boldsymbol{J}_{in} = S_{in} - \frac{\Gamma_{in}}{R}, \quad \boldsymbol{J}_{in} = -D_{in}\nabla n_{in} + n_{in}\mu_{in}\nabla\varphi; \quad (4)$$

$$\frac{\partial n_n}{\partial t} + \nabla\cdot\boldsymbol{J}_n = S_n - n_n\left(D_n/\Lambda^2\right) + \frac{\chi_i Q_T}{M_j}, \quad \boldsymbol{J}_n = -D_n\nabla n_n; \quad (5)$$

$$\varepsilon_0\nabla^2\varphi = -e\left(n_{ip} - n_{in} - n_e\right), \quad (6)$$

where n, $\boldsymbol{J}$, D, μ, S are the number densities, transport fluxes, diffusion coefficients, mobility coefficients, and reaction source terms, respectively. The subscripts e, ε, ip, in, n refer to electrons, electron energy density, positive ions, negative ions, and neutrally charged species, respectively. The electron energy density is defined as $n_\varepsilon = n_e\bar{\varepsilon}$ where $\bar{\varepsilon}$ is the average electron energy. φ is the electrostatic potential; ε_0 is permittivity of free space; and e is elementary charge. Neutral species are assumed to radially diffuse away from the discharge into the remaining vessel through a loss term $n_n(D_n/\Lambda^2)$, where Λ is the characteristic diffusion length, with $(1/\Lambda)^2 = (2.4/R)^2 + (\pi/L)^2$, and R is the discharge radius, consistent with optical emission spectroscopy as 0.25 mm, and L is the inter-electrode gap length [53]. An ambipolar diffusion of charged species into the remaining vessel is assumed. The radial ambipolar flux of positive species, $-D_{ip}n_{ip}/R - n_{ip}\mu_{ip}E_r$, is set equal to the radial flux of negative species, $-D_{ni,e}n_{ni,e}/R + n_{ni,e}\mu_{ni,e}E_r$, along the discharge axis, with the ambipolar field, E_r, solved for in the course of the simulations. The loss term was added to the charged species continuity equations of Γ/R where Γ corresponds to a species ambipolar flux. The total mass flow rate of species radially diffusing away from the discharge is matched by a mass flow rate of species from the remaining vessel diffusing into the discharge. The species diffusing into the discharge are assumed to have the mass fraction corresponding to the initial conditions. The production term $\chi_j Q_T/M_j$ was added to the continuity equation of vessel species j (O_2, H_2, H_2O, and He). Where M_j is the mass of vessel species j, Q_T is the total mass flow of all species diffusing away from the discharge, $\sum(D_n/\Lambda^2)n_nM_n + \sum(\Gamma/R)\,n_{ni,np,e}M_{ni,np,e}$, and χ_j being the fraction of the total mass flow rate into the discharge of species j, $(D_j/\Lambda^2)n_{ji}M_k/\sum(D_j/\Lambda^2)n_{ji}M_k$, where n_{ji} corresponds with the initial densities of background species j.

The local mean energy approximation is used, where the macroscopic electron swarm characteristics vary only with the local average electron energy. Electron transport and reaction coefficients are determined by the solution of the local steady state two-term Boltzmann equation, parameterised over a range of average electron energies [54]. The validity of the local mean energy approximation becomes imprecise at certain times in the discharge evolution. It was found in the modelling that for a short period of time, while the discharge channel spans from the cathode to the anode, and the applied voltage is still high, the sheath electrons become hot (up to 160 eV), and so would 'run away' [54]. Further, the fast time scales of the discharge lead to a greater significance of transient features in the EEDF. As a result of employing the steady state approximation when deriving the electron Boltzmann equation, these transient features of the EEDF were not modelled. It was shown that the rapidly varying electric fields in pulsed discharges, without space charge being considered, can lead to transient EEDF structures that, for example, alter the density of O by around 15% in comparable discharges [55]. Other time-dependent EEDF effects in atmospheric pressure pulsed discharges, for example, occurring as a result of electron–electron collisions, to the authors knowledge, remain uninvestigated in these conditions. The simulations performed here reveal excitation degrees for electronically excited species greater than 1×10^{-4} during the pulse, which is sufficient to alter the EEDF by super-elastic collisions [54]. Finally, the Maxwellianisation of the electron energy distribution function by electron–electron collisions could have a quantitative effect on radical species densities produced during the pulse [53]. Solving the model self-consistently with a more general approach to the electron kinetics would improve the accuracy of the modelling in such discharges. Other considerations relevant to electron kinetics could include gas hydrodynamic effects, as well as a more detailed description of the electron emission from cathode, and the role of gas phase vibrational energy. However, we believe the basic plasma model employed in this work does qualitatively capture the dominant channels of production and losses of O and H.

The reaction kinetic scheme is presented in the appendix with the electron collision cross sections used to determine the transport and reaction coefficients for the electrons. Transport coefficients for ions and electrically neutral heavy species were obtained from [53, 56].

The computation domain used corresponds to the interelectrode dimension, with a length of 2.2 mm. Boundary conditions at the anode describe the absorption of a thermal flux of plasma species and the electron energy density, and a condition describing applied voltage pulses. The boundary conditions used for the plasma species (equations (7)–(9) and (11)–(13) were derived in [57], or can be derived from the same article assuming $D_e = 5/3\, D_{en}$ [54]:

$$\boldsymbol{J}_\mathrm{e} = \boldsymbol{n}\left(\frac{1}{2}\right)\sqrt{\frac{8k_\mathrm{B}T_\mathrm{e}}{\pi m_\mathrm{e}}}n_\mathrm{e}; \tag{7}$$

$$\boldsymbol{J}_\varepsilon = \boldsymbol{n}\left(\frac{5}{6}\right)\sqrt{\frac{8k_\mathrm{B}T_\mathrm{e}}{\pi m_\mathrm{e}}}n_\varepsilon; \tag{8}$$

$$\boldsymbol{J}_\mathrm{ip,in,n} = \boldsymbol{n}S_\mathrm{ip,in,n}\frac{1}{4}\sqrt{\frac{8k_\mathrm{B}T_\mathrm{g}}{\pi m_\mathrm{ip,in,n}}}n_\mathrm{ip,in,n}; \tag{9}$$

$$\varphi = 0.5\,V_0\left(\tanh\left(\nu_\mathrm{rise}\left(t-P_\mathrm{start}\right)\right) - \tanh\left(\nu_\mathrm{fall}\left(t-P_\mathrm{end}\right)\right)\right), \tag{10}$$

where m is the species mass, $\boldsymbol{n}$ is the unit vector facing outwards of the vessel, k_B is the Boltzmann constant, S is the sticking coefficient (with values from [13]). T_e is the electron temperature defined as $2/3\bar{\varepsilon}$, and T_g is the gas temperature, set to 300 K. The voltage pulse waveform shape parameters (V_0, ν_rise, ν_fall, P_start, P_end) were chosen to fit the experimentally measured pulses, where V_0 is the voltage pulse amplitude, ν_rise is the pulse rise time rate, ν_f is the pulse fall time rate, P_start is the pulse start time, and P_end is the pulse end time.

The boundary conditions at the grounded electrode describes the absorption of a thermal flux of plasma species and electron energy density, secondary electron emission, and zero electrostatic potential:

$$\boldsymbol{J}_\mathrm{e} = \boldsymbol{n}\left(\frac{1}{2}\right)\sqrt{\frac{8k_\mathrm{B}T_\mathrm{e}}{\pi m_\mathrm{e}}}n_\mathrm{e} - \gamma\boldsymbol{J}_\mathrm{ip}; \tag{11}$$

$$\boldsymbol{J}_\varepsilon = \boldsymbol{n}\left(\frac{5}{6}\right)\sqrt{\frac{8k_\mathrm{B}T_\mathrm{e}}{\pi m_\mathrm{e}}}n_\varepsilon - \gamma\left(I-2W\right)\boldsymbol{J}_\mathrm{ip}; \tag{12}$$

$$\boldsymbol{J}_\mathrm{ip,in,n} = \boldsymbol{n}S_\mathrm{ip,in,n}\frac{1}{4}\sqrt{\frac{8k_\mathrm{B}T_\mathrm{g}}{\pi m_\mathrm{ip,in,n}}}n_\mathrm{ip,in,n}; \tag{13}$$

$$\varphi = 0, \tag{14}$$

where the secondary emission coefficient, γ, is assumed to characterize all mechanisms of electron emission (due to ion, photon, and excited species bombardment), and was set to 0.25 (by matching modelling and experiment); I corresponds to the energy required for ionisation of a given ion, and W is the work function of the cathode material, set to 4.1 eV [58].

Modelling revealed the build-up of O_2 and H_2 over successive pulses until a quasi-steady state was reached. The steady state values of the presented results of O_2 and H_2 were found by changing the initial conditions of O_2 and H_2 such that the initial and final values of O_2 and H_2, measured in the centre of the discharge, were within 0.5% of each other after a voltage pulse. The initial conditions were 170 ppm of O_2, and 70 ppm of H_2, for 0.1% H_2O, and 190 ppm of O_2, and 75 ppm of H_2 for 0.25% H_2O. The remaining mole fraction was made up by Helium, with trace amounts of the other species. Ten pulses were modelled with the final pulse used in the results presented. The final pulse voltage pulse width was slightly altered in the last pulses (not by more than 3 ns), to achieve a pulse energy of 90 μJ, to match the pulse energy from the experiment.

The plasma model was implemented using the commercial finite element analysis software COMSOL Multiphysics.

4. Spatial and temporal evolution of the density of O and H

The temporal evolution of the density of the ground states of O and H obtained by ps-TALIF and by 1D fluid modelling at mid-gap in He + 0.1% and 0.25% H_2O are presented in figure 3. They demonstrate a reasonable agreement between experiment and modelling, within around a factor of 3 for O and H densities.

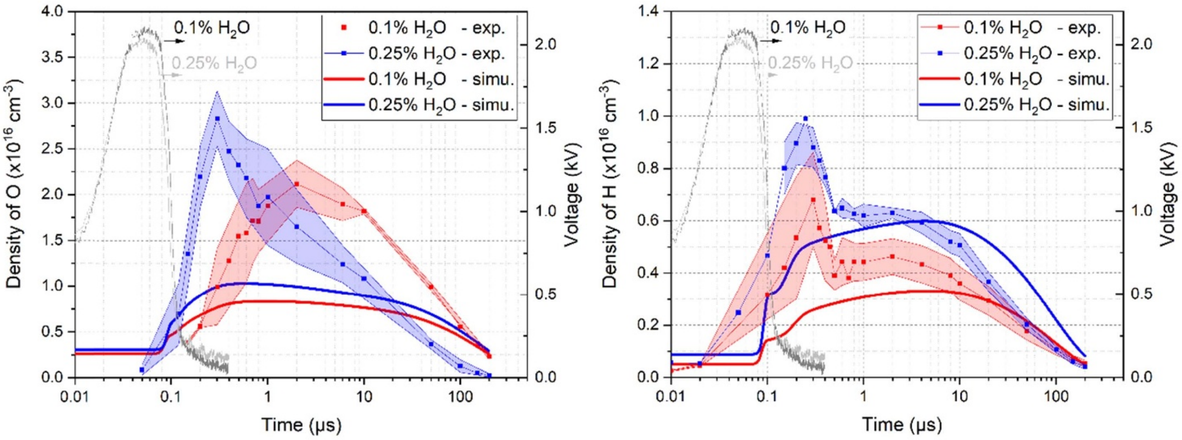

Figure 3. Experimental and numerical results of the temporal evolution of the density of O (left) and H (right) at mid-gap ($U = 2$ kV, $P = 1$ atm, gap = 2.2 mm). Experimental error is based on standard deviation determination only. The other major uncertainties come from the uncertainty of the TALIF cross sections of O and H which are 20% and 50% respectively and of the fluorescence lifetimes determination and the total experimental error is estimated to be 60% and 64% respectively.

4.1. He + 0.1% H_2O

Atomic oxygen is mainly produced during the early post discharge. In the experiments, the density builds up over the first 1–2 μs, then remains nearly constant at about 2×10^{16} cm^{-3} over 10 μs before decreasing on a time scale of 100 μs. The density of H shows a strong production during the discharge followed by a moderate decrease over 200 ns and then, similarly to O, remains constant at about 0.45×10^{16} cm^{-3}, over 10 μs, before decreasing on a time scale of 100 μs. While the density evolution of H in the post discharge is well reproduced by modelling, the fast rise and fall of H during the discharge phase, between 0.1 and 0.4 μs, is underestimated by the model. The authors speculate the rotational and vibrational energy of H_2O, which is not captured by the model, may lead to an increased rate of dissociation of H_2O by electron impact, leading to the faster rise of the H density than is currently predicted in the model.

At increased water vapour concentration, the production of O is enhanced during the pulse, which is reproduced to a lesser extent by modelling. The production processes governing the evolution of H density seem similar at increased water content, only the absolute density of H increases by nearly 40% from 0.1% to 0.25% H_2O.

The production and loss reaction rates of O and H in He + 0.1% H_2O according to the modelling are given in figure 4. They show that the four most significant kinetic processes happen during the discharge and in the early post discharge (<1 μs). Since the relative importance of these processes is quite similar at 0.25% H_2O according to the model, only processes at 0.1% H_2O are shown here. The temporal evolution of the electron temperature obtained by modelling is given in figure 5.

According to the simulation, at 0.1% H_2O, atomic oxygen is dominantly formed through two different processes. As the electron temperature remains high (4–6 eV) during the voltage pulse (up to ~100 ns), electron impact dissociation of O_2 dominates, with molecular oxygen being produced during the previous discharges (density of O_2 at the beginning of the pulse is around 4×10^{21} m^{-3}). As the electron temperature drops down below 0.5 eV, O is then formed through a two-step process: formation of O_2^+ (during the discharge, mainly by charge transfer of He_2^+ and H^+ with O_2), followed by electron–ion dissociative recombination with O_2^+. This process lasts until O_2^+ is totally consumed and is responsible for most of the production of O. It was already pointed out in Bruggeman and Schram [59] that dissociative recombination was an important process for the production of radicals (in that case OH) in atmospheric pressure glow discharges where the electron temperature ranges in 1–2 eV at low gas temperature. The same applies here for O and H (see below for H), all the more as the electron temperature decays down below 0.5 eV since the rate for dissociative recombination is proportional to the inverse of the electron temperature.

The main loss mechanisms of O also vary with the electron temperature. As the latter is still high, 4–6 eV, O is ionised by electron impact to form O^+. Only few O^+ ions will recombine to atomic oxygen, most O^+ ions are lost in the formation of O_2^+. From 100 to 400 ns, charge transfer with He+ and ionisation by excited Helium states dominate but the density of O still rises due to electron–ion recombination. After 400–600 ns, radial diffusion losses largely dominate and lead to the drop of O density after 1–2 μs when the production of O nearly stops. The situation is rather similar for H. During the discharge, H is mainly produced by electron impact dissociation of H_2O and OH and by electron impact dissociation of H_2^+ (density of H_2 at the beginning of the pulse is around 1.7×10^{21} m^{-3} according to modelling). During the early post-discharge, H production is almost entirely due to electron–ion recombination with H_2^+ and H^+. Losses are mainly governed by Penning ionisation and charge transfer reactions with O^+, then by radial losses.

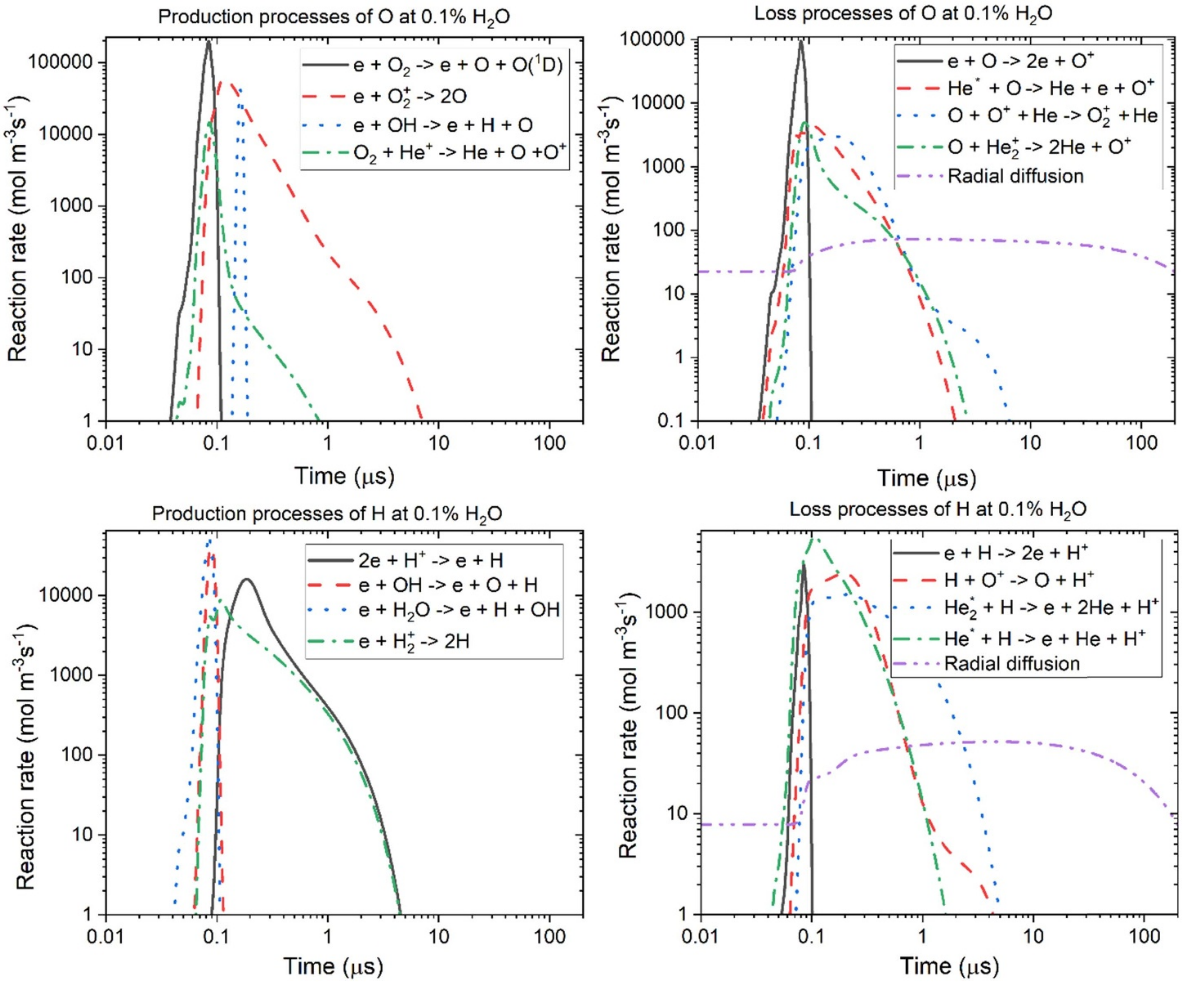

Figure 4. Temporal evolution of the four largest production and loss reaction rates for O (top) and H (bottom) in He + 0.1% H_2O, and rate of radial losses for O and H. HeS and He_2S represent the excited states of He and He_2, treated as an effective excited state in the chemistry set.

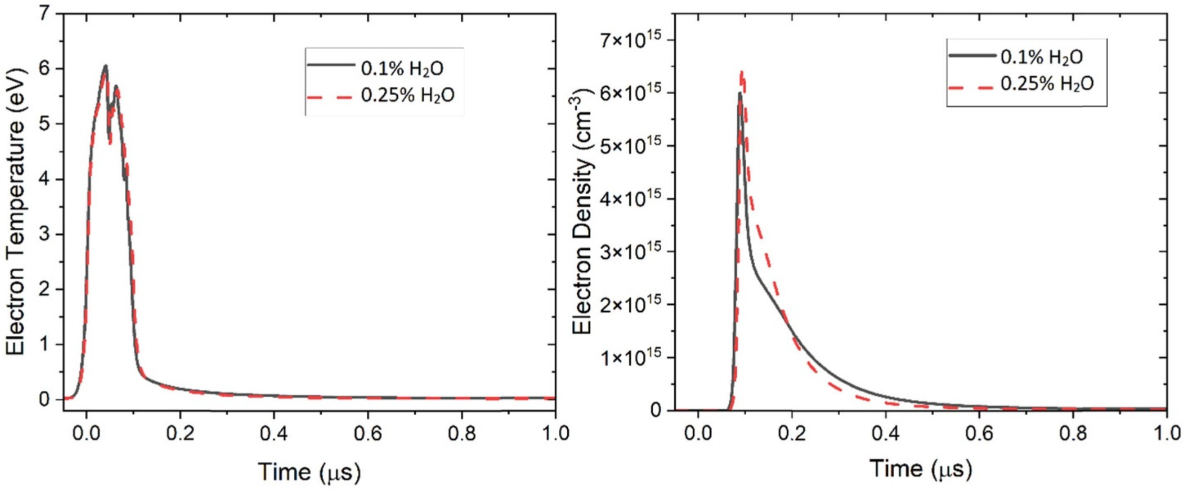

Figure 5. Temporal evolution of the mean electron temperature at mid gap obtained by 1D fluid modelling at 0.1% H_2O.

Neutral kinetics involving O and H happen on longer time scales than radial diffusion. The fastest processes are recombination of O and H with OH, to form O_2 + H and H_2 + O or H_2O, respectively. However, from 1 to 20 μs, the density of OH drops down from 5×10^{20} to 2×10^{19} m^{-3} and the recombination time scale in these conditions is about

60 μs and 1500 μs, respectively. Therefore, once the ion chemistry is finished, the densities of O and H remain relatively constant until it drops due to radial diffusion. This large time window may therefore provide an opportunity to use O and H radicals to produce long-lived species tailored to specific applications. Increased repetition frequency up to 50 kHz would trigger the next discharge before the decrease of the density of O and H radicals, possibly fostering their production.

Finally, we can note that in the conditions presented here, the impact of impurities seems negligible on the formation of atomic oxygen. The concentration of water vapour is sufficient to form significantly more O_2 than what comes from impurities coming from the bottle and the gas lines. Similarly, effects of impurities on an RF atmospheric discharge in He + H_2O were shown to affect the density of O for water concentrations below 0.1% only [19].

4.2. He + 0.25% H_2O

As the water vapour concentration in the feed gas increases, both the discharge properties and the kinetics are affected. Competing effects due to the loss of electrons by attachment processes and increasing electron temperature due to energy losses in inelastic collisions with water molecules, can lead to a complex evolution of the discharge development and reaction rates of electron impact induced reaction. For instance, in He + H_2O RF discharges, changes in the electron properties induce the non-linear rise of OH density with increasing water content [18]. Also, in the negative ns-pulsed discharge studied in [34], humidity affects the discharge ignition due to a competition between a slower discharge propagation at lower initial electron density (left by the previous pulse), leading to a higher channel conductivity at breakdown and a faster return wave and consequently a faster current rise. A similar behaviour may characterise this work (see figure 1).

Figure 3 (left) shows a strong enhancement of the production of O during the discharge phase at 0.25% H_2O. It is reproduced to a lesser extent by modelling. The increased production of O during the discharge is consistent with the dissociation of O_2 by electron impact being the dominant production reaction of O, since the O_2 density produced by the previous pulses increases significantly with H_2O concentration (4.7×10^{21} m^{-3} according to modelling). Also, the modelling suggests an increased reaction rate for the dissociation of OH by electron impact relative to the other processes. The earlier rise of the density of O at 0.25% H_2O is only due to the earlier rise of the current as explained above.

The density of H increases by about 50% as the water concentration increases from 0.1% to 0.25%, while the temporal evolution of the density is unchanged. This could be explained by the fact that H is mainly produced by direct interaction of electrons with water molecules and by He* induced reactions with H, the density of He* being weakly affected by the increase of humidity according to the modelling work of Murakami *et al* [60] in helium–oxygen plasmas with humid-air impurities at atmospheric pressure.

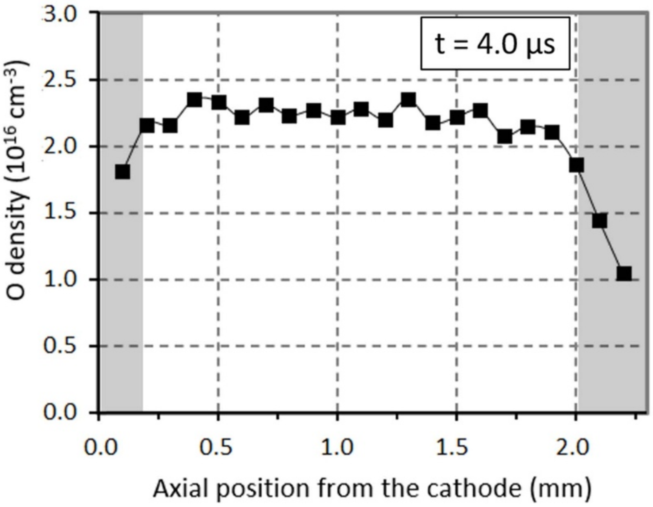

Figure 6. Evolution of the O density along the discharge axis at 4 μs. Grey zones are impacted by loss of TALIF signal by interaction with the electrodes (solid angle of detection, beam profile truncation) and are not studied in detail here.

The build-up of O_2 over successive pulses occurs more quickly with increased H_2O water vapour. The reported modelling finds a factor of 1.2 increase in the average O_2 density at the start of the final pulse, with 0.25% H_2O as opposed to 0.1% H_2O. Given that direct electron impact of O_2 is the main source of O, the build-up O_2 is an important aspect when considering the controllability of O production.

The results and the analysis of the kinetics of O and H done at mid gap are valid along the discharge axis. Indeed, the experimental determination of the density of O along the axis of the discharge at 4.0 μs (done at 0.1% H_2O) is illustrated in figure 6. It demonstrates that the production of O is quasi homogenous within experimental error along the gap.

It should be noted that water clusters are not yet considered in the current model while they could allow for additional pathways to O and H production in the afterglow, similar in nature to the ones identified in this work [28]. This effort will be the topic of a future publication.

5. Conclusion

The spatio-temporal distribution of O and H radicals in a He + H_2O (0.1%–0.25%) nanosecond pulsed discharge was studied experimentally by ps-TALIF and by 1D fluid modelling. The model indicates which reaction pathways achieve the O and H production seen in the experiment, particularly in the afterglow. Most O and H radicals are produced in the early afterglow (up to 1 μs) through recombination processes of O_2^+ and H_2^+. The accurate prediction and optimisation of these radical densities in pulsed discharges therefore requires the consideration of both electron-impact dissociation during the plasma pulse and the additional afterglow processes, mainly dissociative recombination.

Data availability statement

The data that support the findings of this study are openly available at the following URL/DOI: https://pure.york.ac.uk/portal/en/datasets/data-for-psst-paper-2023.

Acknowledgments

The authors acknowledge the support of the Engineering and Physical Science Research Council (Project Nos. EP/S026584/1 and EP/S025790/1)

Appendix

The kinetic scheme used in this work was based on [61], which had reactions involving nitrogen removed. The reactions that involved H_2 and H and the non-nitrogen species from [13], were also included.

Reaction number	Reaction formula	Reaction coefficient	Energy cost (eV)	References
R1	$e + He \rightarrow e + He$	$f(x_{gas}, \varepsilon_{avg})$	Calc.	[62]
R2	$e + He \rightarrow e + He^*$	$f(x_{gas}, \varepsilon_{avg})$	19.80	[62]
R3	$e + He^* \rightarrow e + He$	$1.7633 \times 10^{-16}\ \varepsilon_{avg}{}^{0.31}$	−19.80	[63]
R4	$e + He \rightarrow 2e + He^+$	$f(x_{gas}, \varepsilon_{avg})$	24.58	[62]
R5	$e + He^* \rightarrow 2e + He^+$	$1 \times 10^{-13}\ \varepsilon_{avg}{}^{0.6} \exp(-7.175/\varepsilon_{avg})$	4.78	[63]
R6	$e + O_2 \rightarrow e + O_2$	$f(x_{gas}, \varepsilon_{avg})$	Calc.	[64]
R7	$e + O_2 \rightarrow 2e + O_2{}^+$	$f(x_{gas}, \varepsilon_{avg})$	12.06	[64]
R8	$e + He_2{}^* \rightarrow 2e + He_2{}^+$	$7.28 \times 10^{-16}\ \varepsilon_{avg}{}^{0.71} \exp(-5.1/\varepsilon_{avg})$	3.4	[63]
R9	$e + He_2{}^+ \rightarrow He + He^*$	$6.1382 \times 10^{-15}\ \varepsilon_{avg}{}^{-0.5}$		[63]
R10	$2e + He^+ \rightarrow e + He$	$7 \times 10^{-32}\ T_{eg}{}^{-4.5}$		[65]
R11	$2e + He_2{}^+ \rightarrow e + 2He$	$7 \times 10^{-32}\ T_{eg}{}^{-4.5}$		[65]
R12	$e + He + He_2{}^+ \rightarrow 3He$	$2 \times 10^{-39}\ T_{eg}{}^{-2.5}$		[65]
R13	$e + He^+ \rightarrow He$	2×10^{-18}		[65]
R14	$e + He_2{}^+ \rightarrow 2He$	1×10^{-14}		[65]
R15	$e + O_2{}^+ \rightarrow 2O$	$7.762 \times 10^{-15}\ \varepsilon_{avg}{}^{-1}$	−6.91	[63]
R16	$e + He + He^+ \rightarrow He + He^*$	1×10^{-39}		[65]
R17	$e + He + He_2{}^+ \rightarrow 2He + He^*$	$5 \times 10^{-39}/T_{eg}$		[65]
R18	$e + He + He_2{}^+ \rightarrow He + He_2{}^*$	1.5×10^{-39}		[65]
R19	$2e + He^+ \rightarrow e + He^*$	$6 \times 10^{-32}\ T_{eg}{}^{-4}$		[65]
R20	$2e + He_2{}^+ \rightarrow He + He^* + e$	$1 \times 10^{-32}\ T_{eg}{}^{-4}$		[65]
R21	$2e + He_2{}^+ \rightarrow He_2{}^* + e$	$3 \times 10^{-32}\ T_{eg}{}^{-4}$		[65]
R22	$e + He^+ \rightarrow He^*$	$6.76 \times 10^{-19}\ T_e{}^{-0.5}$		[65]
R23	$e + He_2{}^+ \rightarrow He + He^*$	$8.9 \times 10^{-15}\ T_{eg}{}^{-1.5}$		[65]
R24	$e + H_2O \rightarrow e + H_2O$	$f(x_{gas}, \varepsilon_{avg})$	Calc.	[65]
R25	$e + O_2 \rightarrow O_2{}^-$	$f(x_{gas}, \varepsilon_{avg})$		[65]
R26	$e + H_2O \rightarrow e + H + OH$	$f(x_{gas}, \varepsilon_{avg})$	9	[65]
R27	$e + H_2O \rightarrow O^+ + H_2 + 2e$	$f(x_{gas}, \varepsilon_{avg})$	19	[66]
R28	$e + H_2O \rightarrow OH + H^+ + 2e$	$f(x_{gas}, \varepsilon_{avg})$	16.9	[66]
R29	$e + H_2O \rightarrow O + H_2{}^+ + 2e$	$f(x_{gas}, \varepsilon_{avg})$	20.7	[66]
R30	$e + H_2O \rightarrow H + OH^-$	$f(x_{gas}, \varepsilon_{avg})$		[13]
R31	$e + H \rightarrow H^+ + 2e$	$f(x_{gas}, \varepsilon_{avg})$	13.6	[66]
R32	$e + H_2 \rightarrow H_2{}^+ + 2e$	$f(x_{gas}, \varepsilon_{avg})$	15.96	[66]
R33	$e + H_2 \rightarrow 2H + e$	$f(x_{gas}, \varepsilon_{avg})$	14.68	[66]
R34	$e + H_2{}^+ \rightarrow e + H + H^+$	$1.89 \times 10^{-7}\ T_e{}^{0.5} \exp(-2.3/T_e)$		[66]
R35	$e + H^+ \rightarrow H$	$2.62 \times 10^{-13}\ T_e{}^{0.5}$		[66]
R36	$2e + H^+ \rightarrow e + H$	$8.8 \times 10^{-27}\ T_e{}^{-4.5}$		[66]
R37	$e + H_2{}^+ \rightarrow 2H$	$5.66 \times 10^{-8}\ T_e{}^{-0.6}$		[66]
R38	$e + OH \rightarrow e + O + H$	$2.08 \times 10^{-13}\ T_e{}^{-0.76} \exp(-6.9/T_e)$	6.9	[65]
R39	$2e + O_2{}^+ \rightarrow e + O_2$	$7 \times 10^{-32}\ T_{eg}{}^{-4.5}$		[65]
R40	$e + O_2 + O_2{}^+ \rightarrow 2O_2$	$2.49 \times 10^{-41}\ T_{eg}{}^{-1.5}$		[65]
R41	$e + O_3 \rightarrow O + O_2{}^-$	$5.87 \times 10^{-15}\ T_e{}^{-1.5} \exp(-1.59/T_e)$		[65]
R42	$e + O_3 \rightarrow O_2 + O^-$	$2.12 \times 10^{-15}\ T_e{}^{-1.06} \exp(-0.93/T_e)$		[65]
R43	$e + O^- \rightarrow O + 2e$	$5.47 \times 10^{-14}\ T_e{}^{0.324} \exp(-2.98/T_e)$	2.98	[65]
R44	$e + O_2 \rightarrow 2O + e$	$1.41 \times 10^{-15}\ T_e{}^{0.22} \exp(-12.62/T_e)$	12.62	[65]
R45	$e + O_2 \rightarrow O + O^-$	$1.07 \times 10^{-15}\ T_e{}^{-1.39} \exp(-6.26/T_e)$	6.26	[65]
R46	$e + O_2 + H_2O \rightarrow H_2O + O_2{}^-$	1.4×10^{-41}		[65]
R47	$e + He + O \rightarrow He + O^-$	1×10^{-43}		[65]
R48	$e + He + O_2 \rightarrow He + O_2{}^-$	$3.6 \times 10^{-43}\ T_e{}^{-0.5}$		[65]
R49	$e + He + O_3 \rightarrow He + O_3{}^-$	1×10^{-43}		[65]
R50	$e + O + O_2 \rightarrow O + O_2{}^-$	1×10^{-43}		[65]
R51	$e + O + O_2 \rightarrow O_2 + O^-$	1×10^{-43}		[65]
R52	$e + 2O_2 \rightarrow O_2 + O_2{}^-$	$3.6 \times 10^{-43}\ T_e{}^{-0.5}$		[65]
R53	$e + O_2 + O_3 \rightarrow O_2 + O_3{}^-$	1×10^{-43}		[65]
R54	$e + O^+ \rightarrow O$	4×10^{-18}		[65]

(Continued.)

(Continued.)

Reaction number	Reaction formula	Reaction coefficient	Energy cost (eV)	References
R55	$e + O_2^+ \rightarrow O_2$	4×10^{-18}		[65]
R56	$2e + O^+ \rightarrow O + e$	$7 \times 10^{-32}\ T_{eg}^{-4.5}$		[65]
R57	$e + He + O^+ \rightarrow He + O$	$6 \times 10^{-39}\ T_{eg}^{-2.5}$		[65]
R58	$e + O_2 + O^+ \rightarrow O_2 + O$	$6 \times 10^{-39}\ T_{eg}^{-2.5}$		[65]
R59	$e + O \rightarrow 2e + O^+$	$9 \times 10^{-14}\ T_e^{0.7} \exp(-13.6/T_e)$	13.6	[65]
R60	$e + O_2 \rightarrow 2e + O + O^+$	$5.4 \times 10^{-16}\ T_e^{0.5} \exp(-17/T_e)$	17	[65]
R61	$e + O_2 \rightarrow O^- + e + O^+$	$7.1 \times 10^{-17}\ T_e^{0.5} \exp(-17/T_e)$	17	[65]
R62	$e + H \rightarrow e + H$	$f(x_{gas}, \varepsilon_{avg})$	Calc.	[66]
R63	$e + H_2 \rightarrow e + H_2$	$f(x_{gas}, \varepsilon_{avg})$	Calc.	[66]
R64	$e + OH \rightarrow OH^-$	1×10^{-21}		[65]
R65	$e + OH + He \rightarrow He + OH^-$	3×10^{-43}		[65]
R66	$He^* + 2He \rightarrow He_2^* + He$	1.3×10^{-45}		[63]
R67	$2He + He^+ \rightarrow He + He_2^+$	1×10^{-43}		[63]
R68	$2He^* \rightarrow He + e + He^+$	2.7×10^{-16}		[65]
R69	$O_2 + He^+ \rightarrow He + O_2^+$	$3.3 \times 10^{-17}\ T_g^{0.5}$		[65]
R70	$He^* + He_2^+ \rightarrow 2He + He^+$	1×10^{-16}		[65]
R71	$O_2 + He_2^+ \rightarrow 2He + O_2^+$	$1 \times 10^{-15}\ T_g^{0.5}$		[65]
R72	$2O_2 \rightarrow 2O + O_2$	$6.6 \times 10^{-15}\ T_0^{-1.5} \exp(-59\,000/T_g)$		[65]
R73	$He^* + He + O_2 \rightarrow 2He + e + O_2^+$	1.6×10^{-43}		[65]
R74	$He^* + O_2 \rightarrow He + e + O_2^+$	2.6×10^{-16}		[65]
R75	$2O \rightarrow O_2$	$9.26 \times 10^{-40}\ T_0^{-1}$		[65]
R76	$3O \rightarrow O_2 + O$	$9.21 \times 10^{-46}\ T_0^{-0.63}$		[65]
R77	$2O + O_2 \rightarrow 2O_2$	$2.56 \times 10^{-46}\ T_0^{-0.63}$		[65]
R78	$2O + H_2O \rightarrow O_2 + H_2O$	$1.7 \times 10^{-44}\ T_0^{-1}$		[65]
R79	$O_2^- + He^+ \rightarrow O_2 + He$	$2 \times 10^{-13}\ T_0^{-1}$		[65]
R80	$O_2^- + He_2^+ \rightarrow 2He + O_2$	1×10^{-13}		[65]
R81	$O_2^- + O_2^+ \rightarrow 2O + O_2$	1×10^{-13}		[65]
R82	$O_2^- + O_2^+ \rightarrow 2O_2$	$4.2 \times 10^{-13}\ T_0^{-0.5}$		[65]
R83	$O_2^- + He + He_2^+ \rightarrow 3He + O_2$	$2 \times 10^{-37}\ T_0^{-2.5}$		[65]
R84	$O_2^- + O_2 + He_2^+ \rightarrow 2He + 2O_2$	$2 \times 10^{-37}\ T_0^{-2.5}$		[65]
R85	$He + O_2^- \rightarrow He + O_2 + e$	$3.9 \times 10^{-16} \exp(-7400/T_g)$		[65]
R86	$He^* + O_2^- \rightarrow He + O_2 + e$	3×10^{-16}		[65]
R87	$He_2^* + O_2^- \rightarrow 2He + O_2 + e$	3×10^{-16}		[65]
R88	$O_2 + O_2^- \rightarrow 2O_2 + e$	$2.7 \times 10^{-16}\ T_0^{0.5} \exp(-5590/T_g)$		[65]
R89	$H_2O + O_2^- \rightarrow H_2O + O_2 + e$	$5 \times 10^{-15} \exp(-5000/T_g)$		[65]
R90	$2He^* \rightarrow e + He_2^+$	1.05×10^{-15}		[65]
R91	$He_2^* + He^* \rightarrow 2He + e + He^+$	5×10^{-16}		[65]
R92	$He_2^* + He^* \rightarrow He + e + He_2^+$	2×10^{-15}		[65]
R93	$2He_2^* \rightarrow 3He + e + He^+$	3×10^{-16}		[65]
R94	$2He_2^* \rightarrow 2He + e + He_2^+$	1.2×10^{-15}		[65]
R95	$2He + He^* \rightarrow He + He_2^*$	1.5×10^{-46}		[65]
R96	$2O + He \rightarrow O_2 + He$	1×10^{-45}		[65]
R97	$O_2^- + He + O_2^+ \rightarrow He + 2O_2$	$2 \times 10^{-37}\ T_0^{-2.5}$		[65]
R98	$O_2^- + O_2 + O_2^+ \rightarrow 3O_2$	$2 \times 10^{-37}\ T_0^{-2.5}$		[65]
R99	$He_2^* + O_2 \rightarrow 2He + e + O_2^+$	3.6×10^{-16}		[65]
R100	$OH + O \rightarrow O_2 + H$	$2.2 \times 10^{-17} \exp(120/T_g)$		[65]
R101	$O + H_2O \rightarrow 2OH$	$2.5 \times 10^{-20}\ T_0^{1.14} \exp(-8624/T_g)$		[65]
R102	$2OH \rightarrow H_2O + O$	$4.2 \times 10^{-18} \exp(-240/T_g)$		[65]
R103	$H + OH + H_2O \rightarrow 2H_2O$	$2.46 \times 10^{-42}\ T_0^{-2}$		[65]
R104	$H + OH + O_2 \rightarrow H_2O + O_2$	$6.88 \times 10^{-43}\ T_0^{-2}$		[65]
R105	$O + H + H_2O \rightarrow H_2O + OH$	$2.76 \times 10^{-44}\ T_0^{-1}$		[65]
R106	$H + OH + He \rightarrow H_2O + He$	$1.56 \times 10^{-43}\ T_0^{-2.6}$		[65]
R107	$O_2 + H \rightarrow O + OH$	$3.7 \times 10^{-16} \exp(-8455/T_g)$		[65]
R108	$O^- + He + O_2^+ \rightarrow O + O_2 + He$	$2 \times 10^{-37}\ T_0^{-2.5}$		[65]
R109	$O^- + O_2 + O_2^+ \rightarrow O + 2O_2$	$2 \times 10^{-37}\ T_0^{-2.5}$		[65]
R110	$O^- + O_2 + O_2^+ \rightarrow O_2 + O_3$	$2 \times 10^{-37}\ T_0^{-2.5}$		[65]

(Continued.)

(Continued.)

R111	$2O_3 \rightarrow O + O_2 + O_3$	$1.6 \times 10^{-15} \exp(-11\,400/T_g)$	[65]
R112	$O_3 + H_2O \rightarrow O + O_2 + H_2O$	$1.6 \times 10^{-15} \exp(-11\,400/T_g)$	[65]
R113	$O_3 + H \rightarrow O_2 + OH$	$7.78 \times 10^{-17}\ T_0^{0.25} \exp(-327.8/T_g)$	[65]
R114	$O_3 + O_2 \rightarrow O + 2O_2$	$1.6 \times 10^{-15} \exp(-11\,400/T_g)$	[65]
R115	$O_3 + O \rightarrow 2O + O_2$	$9.4 \times 10^{-17} \exp(-11\,400/T_g)$	[65]
R116	$O_3 + O \rightarrow 2O_2$	$8 \times 10^{-18} \exp(-2060/T_g)$	[65]
R117	$2O + O_2 \rightarrow O_3 + O$	$3.4 \times 10^{-46}\ T_0^{-1.2}$	[65]
R118	$O + 2O_2 \rightarrow O_3 + O_2$	$6 \times 10^{-46}\ T_0^{-2.8}$	[65]
R119	$O + O_2 + O_3 \rightarrow 2O_3$	$2.3 \times 10^{-47} \exp(-1057/T_g)$	[65]
R120	$O + O_2 + He \rightarrow He + O_3$	$3.4 \times 10^{-46}\ T_0^{-1.2}$	[65]
R121	$O^- + O_2^+ \rightarrow 3O$	1×10^{-13}	[65]
R122	$O^- + O_2^+ \rightarrow O + O_2$	$1 \times 10^{-13}\ T_0^{-0.5}$	[65]
R123	$O^- + He^+ \rightarrow O + He$	$2 \times 10^{-13}\ T_0^{-1}$	[65]
R124	$O^- + He_2^+ \rightarrow O + 2He$	1×10^{-13}	[65]
R125	$O^- + He + He^+ \rightarrow 2He + O$	$2 \times 10^{-37}\ T_0^{-2.5}$	[65]
R126	$O^- + O_2 + He^+ \rightarrow He + O + O_2$	$2 \times 10^{-37}\ T_0^{-2.5}$	[65]
R127	$O^- + He + He_2^+ \rightarrow 3He + O$	$2 \times 10^{-37}\ T_0^{-2.5}$	[65]
R128	$O^- + O_2 + He_2^+ \rightarrow 2He + O + O_2$	$2 \times 10^{-37}\ T_0^{-2.5}$	[65]
R129	$O^- + He \rightarrow He + O + e$	$2.5 \times 10^{-24}\ T_0^{0.6}$	[65]
R130	$O^- + He^* \rightarrow He + O + e$	3×10^{-16}	[65]
R131	$O^- + He_2^* \rightarrow 2He + O + e$	3×10^{-16}	[65]
R132	$O^- + O \rightarrow O_2 + e$	$2 \times 10^{-16}\ T_0^{0.5}$	[65]
R133	$O^- + O_2 \rightarrow O + O_2^-$	1.5×10^{-18}	[65]
R134	$O^- + O_2 \rightarrow O_3 + e$	$5 \times 10^{-21}\ T_0^{0.5}$	[65]
R135	$O^- + O_3 \rightarrow 2O_2 + e$	$3.01 \times 10^{-16}\ T_0^{0.5}$	[65]
R136	$O^- + H \rightarrow OH + e$	5×10^{-16}	[65]
R137	$O_2^- + O \rightarrow O_2 + O^-$	$1.5 \times 10^{-16}\ T_0^{0.5}$	[65]
R138	$O_2^- + O \rightarrow O_3 + e$	$1.5 \times 10^{-16}\ T_0^{0.5}$	[65]
R139	$He + O_3 \rightarrow He + O + O_2$	$1.56 \times 10^{-15} \exp(-11\,400/T_g)$	[65]
R140	$He^* + O_3 \rightarrow He + O + e + O_2^+$	2.6×10^{-16}	[65]
R141	$He_2^* + O_3 \rightarrow 2He + O + e + O_2^+$	3.6×10^{-16}	[65]
R142	$O^- + O_3 \rightarrow O + O_3^-$	$1.99 \times 10^{-16}\ T_0^{0.5}$	[65]
R143	$O_2^- + O_2 \rightarrow O + O_3^-$	3.5×10^{-21}	[65]
R144	$O_2^- + O_3 \rightarrow O_2 + O_3^-$	$6 \times 10^{-16}\ T_0^{0.5}$	[65]
R145	$O_3^- + He \rightarrow He + O + O_2 + e$	3×10^{-16}	[65]
R146	$O_3^- + He^* \rightarrow He + O_3 + e$	3×10^{-16}	[65]
R147	$O_3^- + He_2^* \rightarrow 2He + O + O_2 + e$	3×10^{-16}	[65]
R148	$O_3^- + O \rightarrow 2O_2 + e$	1×10^{-17}	[65]
R149	$O_3^- + O \rightarrow O_2 + O_2^-$	$2.5 \times 10^{-16}\ T_0^{0.5}$	[65]
R150	$O_3^- + O_2^+ \rightarrow 2O + O_3$	1×10^{-13}	[65]
R151	$O_3^- + O_2^+ \rightarrow O_2 + O_3$	$2 \times 10^{-13}\ T_0^{-1}$	[65]
R152	$O_3^- + He + He_2^+ \rightarrow 3He + O_3$	$2 \times 10^{-37}\ T_0^{-2.5}$	[65]
R153	$O_3^- + O_2 + He_2^+ \rightarrow 2He + O_3 + O_2$	$2 \times 10^{-37}\ T_0^{-2.5}$	[65]
R154	$O_3^- + O_3 \rightarrow 3O_2 + e$	1×10^{-16}	[65]
R155	$O^- + 2O_2 \rightarrow O_2 + O_3^-$	$1.1 \times 10^{-42}\ T_0^{-1}$	[65]
R156	$O^- + He + O_2 \rightarrow He + O_3^-$	$1 \times 10^{-42}\ T_0^{-1}$	[65]
R157	$O + He^+ \rightarrow He + O^+$	$5 \times 10^{-17}\ T_0^{0.5}$	[65]
R158	$O_2 + He^+ \rightarrow He + O + O^+$	$1.07 \times 10^{-15}\ T_0^{0.5}$	[65]
R159	$O_3 + He^+ \rightarrow He + O_2 + O^+$	$1.07 \times 10^{-15}\ T_0^{0.5}$	[65]
R160	$OH + He^+ \rightarrow He + H + O^+$	1.1×10^{-15}	[65]
R161	$O + He_2^+ \rightarrow 2He + O^+$	$1 \times 10^{-15}\ T_0^{0.5}$	[65]
R162	$O_2 + He_2^+ \rightarrow 2He + O + O^+$	1.05×10^{-15}	[65]
R163	$O_3 + He_2^+ \rightarrow 2He + O_2 + O^+$	$1 \times 10^{-15}\ T_0^{0.5}$	[65]
R164	$O_2 + O^+ \rightarrow O + O_2^+$	$2 \times 10^{-17}\ T_0^{-0.4}$	[65]
R165	$O_3 + O^+ \rightarrow O_2 + O_2^+$	1×10^{-16}	[65]
R166	$OH + O^+ \rightarrow H + O_2^+$	3.6×10^{-16}	[65]
R167	$He^* + O_2^+ \rightarrow O + He + O^+$	1×10^{-26}	[65]

(Continued.)

(Continued.)

Reaction number	Reaction formula	Reaction coefficient	Energy cost (eV)	References
R168	$He_2^* + O_2^+ \rightarrow O + 2He + O^+$	1×10^{-16}		[65]
R169	$He_2^* + He \rightarrow 3He$	4.9×10^{-22}		[65]
R170	$He^* + O \rightarrow He + e + O^+$	2.6×10^{-16}		[65]
R171	$O + He + O^+ \rightarrow He + O_2^+$	$1 \times 10^{-41}\ T_0^{0.5}$		[65]
R172	$O + O_2 + O^+ \rightarrow O_2 + O_2^+$	$1 \times 10^{-41}\ T_0^{0.5}$		[65]
R173	$He + He^* + O \rightarrow 2He + e + O^+$	1×10^{-43}		[65]
R174	$He + He^* + O_3 \rightarrow 2He + O + e + O_2^+$	1.6×10^{-43}		[65]
R175	$He + O + H \rightarrow He + OH$	$3.2 \times 10^{-45}\ T_0^{-1}$		[65]
R176	$O^- + O^+ \rightarrow 2O$	$2.7 \times 10^{-13}\ T_0^{-0.5}$		[65]
R177	$O_2^- + O^+ \rightarrow O + O_2$	$2 \times 10^{-13}\ T_0^{-1}$		[65]
R178	$O_3^- + O^+ \rightarrow O + O_3$	$2 \times 10^{-13}\ T_0^{-1}$		[65]
R179	$O^- + He + O^+ \rightarrow He + 2O$	$2 \times 10^{-37}\ T_0^{-2.5}$		[65]
R180	$O^- + O_2 + O^+ \rightarrow O_2 + 2O$	$2 \times 10^{-37}\ T_0^{-2.5}$		[65]
R181	$O^- + O_2 + O^+ \rightarrow 2O_2$	$2 \times 10^{-37}\ T_0^{-2.5}$		[65]
R182	$O_2^- + He + O^+ \rightarrow He + O + O_2$	$2 \times 10^{-37}\ T_0^{-2.5}$		[65]
R183	$O_2^- + O_2 + O^+ \rightarrow 2O_2 + O$	$2 \times 10^{-37}\ T_0^{-2.5}$		[65]
R184	$O_2^- + O_2 + O^+ \rightarrow O_2 + O_3$	$2 \times 10^{-37}\ T_0^{-2.5}$		[65]
R185	$O_3^- + He + O^+ \rightarrow He + O + O_2$	$2 \times 10^{-37}\ T_0^{-2.5}$		[65]
R186	$O_3^- + O_2 + O^+ \rightarrow O_3 + O + O_2$	$2 \times 10^{-37}\ T_0^{-2.5}$		[65]
R187	$O_3^- + He + O_2^+ \rightarrow O_3 + He + O_2$	$2 \times 10^{-37}\ T_0^{-2.5}$		[65]
R188	$O_3^- + O_2 + O_2^+ \rightarrow O_3 + 2O_2$	$2 \times 10^{-37}\ T_0^{-2.5}$		[65]
R189	$OH^- + He \rightarrow He + OH + e$	$2 \times 10^{-15}\ \exp(-24\,030/T_g)$		[66]
R190	$OH^- + H \rightarrow H_2O + e$	1.8×10^{-15}		[66]
R191	$O^- + H_2O \rightarrow OH + OH^-$	1.4×10^{-15}		[66]
R192	$OH^- + He_2^+ \rightarrow OH + 2He$	1×10^{-13}		[66]
R193	$OH^- + O_2^+ \rightarrow OH + O_2$	$2 \times 10^{-13}\ T_0^{-0.5}$		[66]
R194	$M + OH^- + He_2^+ \rightarrow 2He + OH + M$	$2 \times 10^{-37}\ T_0^{-2.5}$		[66]
R195	$H + O^+ \rightarrow O + H^+$	6.8×10^{-16}		[66]
R196	$H^+ + O^- \rightarrow O + H$	$2 \times 10^{-13}\ T_0^{-0.5}$		[66]
R197	$O^- + H_2 \rightarrow H_2O + e$	$6 \times 10^{-16}\ T_0^{-0.24}$		[66]
R198	$He^+ + H \rightarrow H^+ + He$	1.9×10^{-21}		[66]
R199	$He^+ + H_2 \rightarrow H^+ + H + He$	$3.7 \times 10^{-20}\ \exp(-35/T_g)$		[66]
R200	$He^+ + H_2 \rightarrow H_2^+ + He$	7.2×10^{-21}		[66]
R201	$He^+ + H_2O \rightarrow H^+ + OH + He$	2.04×10^{-16}		[66]
R202	$He_2^+ + H \rightarrow H^+ + 2He$	3.5×10^{-16}		[66]
R203	$He_2^+ + H_2 \rightarrow H_2^+ + 2He$	3.5×10^{-16}		[66]
R204	$He_2^+ + H_2O \rightarrow O^+ + H_2 + 2He$	2.1×10^{-16}		[66]
R205	$He_2^+ + H_2O \rightarrow H^+ + OH + 2He$	2.1×10^{-16}		[66]
R206	$He_2^+ + H_2O \rightarrow H_2^+ + O + 2He$	2.1×10^{-16}		[66]
R207	$H^+ + H + M \rightarrow H_2^+ + M$	2.1×10^{-44}		[66]
R208	$H^+ + O \rightarrow O^+ + H$	$7 \times 10^{-16}\ \exp(-232/T_g)$		[66]
R209	$H^+ + O_2 \rightarrow O_2^+ + H$	2×10^{-15}		[66]
R210	$H + H_2^+ \rightarrow H^+ + H_2$	6.39×10^{-16}		[66]
R211	$O_2 + H_2^+ \rightarrow O_2^+ + H_2$	8×10^{-16}		[66]
R212	$H_2 + O^- \rightarrow OH^- + H$	3.6×10^{-16}		[66]
R213	$H^+ + OH^- + M \rightarrow H_2O + M$	$2 \times 10^{-37}\ T_0^{-2.5}$		[66]
R214	$H_2^+ + O^- \rightarrow H_2O$	$2 \times 10^{-13}\ T_0^{-0.5}$		[66]
R215	$H_2^+ + O_2^- \rightarrow H_2 + O_2$	$2 \times 10^{-13}\ T_0^{-0.5}$		[66]
R216	$H_2^+ + OH^- \rightarrow H_2O + H$	1×10^{-13}		[66]
R217	$He^* + H \rightarrow H^+ + He + e$	1.1×10^{-15}		[66]
R218	$He^* + H_2 \rightarrow H_2^+ + He + e$	2.9×10^{-17}		[66]
R219	$He_2^* + H \rightarrow 2He + H^+ + e$	2.2×10^{-16}		[66]
R220	$He_2^* + H_2 \rightarrow 2He + H_2^+ + e$	2.2×10^{-16}		[66]
R221	$He^* + H_2 \rightarrow He + 2H$	1.4×10^{-17}		[66]
R222	$He + 2H \rightarrow He + H_2$	$5.8 \times 10^{-45}\ T_0^{-1}$		[66]
R223	$He + H + OH \rightarrow He + H_2O$	$1.56 \times 10^{-43}\ T_0^{-2.6}$		[66]
R224	$2H \rightarrow H_2$	$6.04 \times 10^{-39}\ T_0^{-1}$		[66]

(Continued.)

(Continued.)

R225	$H + O \rightarrow OH$	$4.36 \times 10^{-38}\ T_0{}^{-1}$	[66]
R226	$H + OH \rightarrow O + H_2$	$8 \times 10^{-27}\ T_g{}^{2.8}\ \exp(-1950/T_g)$	[66]
R227	$H + OH \rightarrow H_2O$	$8 \times 10^{-27}\ T_g{}^{2.8}\ \exp(-1950/T_g)$	[66]
R228	$3H \rightarrow H + H_2$	$6 \times 10^{-43}\ T_0{}^{-1}$	[66]
R229	$2H + H_2 \rightarrow 2H_2$	$8.1 \times 10^{-45}\ T_0{}^{-0.6}$	[66]
R230	$2H + H_2O \rightarrow H_2O + H_2$	$1.32 \times 10^{-43}\ T_0{}^{-1.25}$	[66]
R231	$H + O + H_2 \rightarrow OH + H_2$	$9.19 \times 10^{-45}\ T_0{}^{-1}$	[66]
R232	$H + OH + H_2 \rightarrow H_2O + H_2$	$4.92 \times 10^{-43}\ T_0{}^{-2}$	[66]
R233	$O + H_2 \rightarrow OH + H$	$3 \times 10^{-20}\ T_g\ \exp(-4480/T_g)$	[66]
R234	$2O + H_2 \rightarrow H_2 + O_2$	$2.65 \times 10^{-45}\ T_0{}^{-1}$	[66]
R235	$H_2 + OH \rightarrow H + H_2O$	$5.3 \times 10^{-22}\ T_g{}^{1.47}\ \exp(-1761/T_g)$	[66]
R236	$H_2 + H_2O \rightarrow OH + H + H_2$	$5.8 \times 10^{-15}\ \exp(52\,900/T_g)$	[66]

All rate coefficients have volume units of $m^3\ s^{-1}$ for two body reactions and $m^6\ s^{-1}$ for three body. ε_{avg}, defined as $3/2T_e$, is the average electron energy in eV, x_{gas} is the initial mole fraction, T_e is the electron temperature in eV, T_{eg} is the electron temperature normalized to the gas temperature ($T_{eg} = T_e/T_g$), and $T_0 = T$[K]/300 K is the normalized gas temperature. Rate coefficients for O_2 and H_2 electron impact reactions were calculated assuming a Maxwellian EEDF. Electronically excited states of O_2 and O were assumed to instantaneously deexcite. He^* represents the groups $He(2^3S)$ and $He(2^1S)$. He_2^* represents $He_2(a^3\sum_u^+)$.

ORCID iDs

Alexandra Brisset https://orcid.org/0000-0003-3217-1106
Matthew Bieniek https://orcid.org/0000-0001-5847-2228
Laurent Invernizzi https://orcid.org/0000-0003-4525-8921
Mohammad Hasan https://orcid.org/0000-0001-6993-933X
James Walsh https://orcid.org/0000-0002-6318-0892
Kari Niemi https://orcid.org/0000-0001-6134-1974
Erik Wagenaars https://orcid.org/0000-0002-5493-3434

References

[1] Brandenburg R, Bruggeman P J and Starikovskaia S M 2017 Fast pulsed discharges *Plasma Sources Sci. Technol.* **26** 020201

[2] Pai D Z, (Ken) Ostrikov K, Kumar S, Lacoste D A, Levchenko I and Laux C O 2013 Energy efficiency in nanoscale synthesis using nanosecond plasmas *Sci. Rep.* **3** 1221

[3] Starikovskii A Y, Anikin N B, Kosarev I N, Mintoussov E I, Nudnova M M, Rakitin A E, Roupassov D V, Starikovskaia S M and Zhukov V P 2008 Nanosecond-pulsed discharges for plasma-assisted combustion and aerodynamics *J. Propuls. Power* **24** 1182–97

[4] Starikovskaia S M 2014 Plasma-assisted ignition and combustion: nanosecond discharges and development of kinetic mechanisms *J. Phys. D: Appl. Phys.* **47** 353001

[5] Sakudo A, Yagyu Y and Onodera T 2019 Disinfection and sterilization using plasma technology: fundamentals and future perspectives for biological applications *Int. J. Mol. Sci.* **20** 5216

[6] Naidis G V, Tarasenko V F, Babaeva N Y and Lomaev M I 2018 Subnanosecond breakdown in high-pressure gases *Plasma Sources Sci. Technol.* **27** 013001

[7] Tarasenko V F, Baksht E H, Burachenko A G, Kostyrya I D, Lomaev M I and Rybka D V 2009 Runaway electrons preionized diffuse discharges at high pressure *2009 IEEE Pulsed Power Conf. 2009 IEEE Pulsed Power Conf.* pp 460–5

[8] Babich L P, Loĭko T V and Tsukerman V A 1990 High-voltage nanosecond discharge in a dense gas at a high overvoltage with runaway electrons *Sov. Phys.-Usp.* **33** 521

[9] Tardiveau P, Magne L, Marode E, Ouaras K, Jeanney P and Bournonville B 2016 Sub-nanosecond time resolved light emission study for diffuse discharges in air under steep high voltage pulses *Plasma Sources Sci. Technol.* **25** 054005

[10] Brisset A, Gazeli K, Magne L, Pasquiers S, Jeanney P, Marode E and Tardiveau P 2019 Modification of the electric field distribution in a diffuse streamer-induced discharge under extreme overvoltage *Plasma Sources Sci. Technol.* **28** 055016

[11] Walsh J L, Shi J J and Kong M G 2006 Contrasting characteristics of pulsed and sinusoidal cold atmospheric plasma jets *Appl. Phys. Lett.* **88** 171501

[12] Luo Y, Lietz A M, Yatom S, Kushner M J and Bruggeman P J 2018 Plasma kinetics in a nanosecond pulsed filamentary discharge sustained in Ar–H_2O and H_2O *J. Phys. D: Appl. Phys.* **52** 044003

[13] Liu D X, Bruggeman P, Iza F, Rong M Z and Kong M G 2010 Global model of low-temperature atmospheric-pressure He + H_2O plasmas *Plasma Sources Sci. Technol.* **19** 025018

[14] Anokhin E M, Popov M A, Kochetov I V, Starikovskiy A Y and Aleksandrov N L 2016 Kinetic mechanism of plasma recombination in methane, ethane and propane after high-voltage nanosecond discharge *Plasma Sources Sci. Technol.* **25** 044006

[15] Mededovic S and Locke B R 2007 Primary chemical reactions in pulsed electrical discharge channels in water *J. Phys. D: Appl. Phys.* **40** 7734–46

[16] Heijkers S, Martini L M, Dilecce G, Tosi P and Bogaerts A 2019 Nanosecond pulsed discharge for CO_2 conversion: kinetic modeling to elucidate the chemistry and improve the performance *J. Phys. Chem.* C **123** 12104–16

[17] Liu D X, Iza F, Wang X H, Kong M G and Rong M Z 2011 He+O_2+H_2O plasmas as a source of reactive oxygen species *Appl. Phys. Lett.* **98** 221501

[18] Schröter S *et al* 2018 Chemical kinetics in an atmospheric pressure helium plasma containing humidity *Phys. Chem. Chem. Phys.* **20** 24263–86

[19] Brisset A, Gibson A R, Schröter S, Niemi K, Booth J-P, Gans T, O'Connell D and Wagenaars E 2021 Chemical kinetics and density measurements of OH in an atmospheric

pressure He + O_2 + H_2O radiofrequency plasma *J. Appl. Phys.* **54** 285201

[20] Murakami T, Niemi K, Gans T, O'Connell D and Graham W G 2014 Afterglow chemistry of atmospheric-pressure helium–oxygen plasmas with humid air impurity *Plasma Sources Sci. Technol.* **23** 025005

[21] Naidis G V 2014 Production of active species in cold helium–air plasma jets *Plasma Sources Sci. Technol.* **23** 065014

[22] Naidis G V 2013 Modelling of OH production in cold atmospheric-pressure He–H_2O plasma jets *Plasma Sources Sci. Technol.* **22** 035015

[23] Reuter S, Winter J, Schmidt-Bleker A, Tresp H, Hammer M U and Weltmann K-D 2012 Controlling the ambient air affected reactive species composition in the effluent of an argon plasma jet *IEEE Trans. Plasma Sci.* **40** 2788–94

[24] Babaeva N Y and Kushner M J 2014 Interaction of multiple atmospheric-pressure micro-plasma jets in small arrays: He/O_2 into humid air *Plasma Sources Sci. Technol.* **23** 015007

[25] Norberg S A, Johnsen E and Kushner M J 2015 Formation of reactive oxygen and nitrogen species by repetitive negatively pulsed helium atmospheric pressure plasma jets propagating into humid air *Plasma Sources Sci. Technol.* **24** 035026

[26] Ono R and Tokuhiro M 2020 Spatiotemporal measurement of OH density from upstream to downstream in humid helium atmospheric-pressure plasma jet *Plasma Sources Sci. Technol.* **29** 035021

[27] McKay K, Liu D X, Rong M Z, Iza F and Kong M G 2012 Generation and loss of reactive oxygen species in low-temperature atmospheric-pressure RF He + O_2 + H_2O plasmas *J. Phys. D: Appl. Phys.* **45** 172001

[28] Schröter S, Bredin J, Gibson A R, West A, Dedrick J P, Wagenaars E, Niemi K, Gans T and O'Connell D 2020 The formation of atomic oxygen and hydrogen in atmospheric pressure plasmas containing humidity: picosecond two-photon absorption laser induced fluorescence and numerical simulations *Plasma Sources Sci. Technol.* **29** 105001

[29] Niemi K, Gathen V S D and Döbele H F 2005 Absolute atomic oxygen density measurements by two-photon absorption laser-induced fluorescence spectroscopy in an RF-excited atmospheric pressure plasma jet *Plasma Sources Sci. Technol.* **14** 375–86

[30] Reuter S, Niemi K, Gathen V S D and Döbele H F 2008 Generation of atomic oxygen in the effluent of an atmospheric pressure plasma jet *Plasma Sources Sci. Technol.* **18** 015006

[31] Waskoenig J, Niemi K, Knake N, Graham L M, Reuter S, Gathen V S D and Gans T 2010 Atomic oxygen formation in a radio-frequency driven micro-atmospheric pressure plasma jet *Plasma Sources Sci. Technol.* **19** 045018

[32] Verreycken T, Horst R M V D, Baede A H F M, Veldhuizen E M V and Bruggeman P J 2012 Time and spatially resolved LIF of OH in a plasma filament in atmospheric pressure He–H_2O *J. Phys. D: Appl. Phys.* **45** 045205

[33] Gianella M, Reuter S, Press S A, Schmidt-Bleker A, Helden J H V and Ritchie G A D 2018 HO_2 reaction kinetics in an atmospheric pressure plasma jet determined by cavity ring-down spectroscopy *Plasma Sources Sci. Technol.* **27** 095013

[34] Brisset A, Harris B, Dickenson A, Niemi K, Walsh J and Wagenaars E 2022 Effects of humidity on the dynamics and electron recombination of a pin-to-pin discharge in He + H_2O at atmospheric pressure *Plasma Sources Sci. Technol.* **31** 045008

[35] Simeni M S, Roettgen A, Petrishchev V, Frederickson K and Adamovich I V 2016 Electron density and electron temperature measurements in nanosecond pulse discharges over liquid water surface *Plasma Sources Sci. Technol.* **25** 064005

[36] Marode E 1975 The mechanism of spark breakdown in air at atmospheric pressure between a positive point and a plane. I. Experimental: nature of the streamer track *J. Appl. Phys.* **46** 2005–15

[37] Spyrou N and Manassis C 1989 Spectroscopic study of a positive streamer in a point-to-plane discharge in air: evaluation of the electric field distribution *J. Phys. D: Appl. Phys.* **22** 120–8

[38] Stancu G D 2020 Two-photon absorption laser induced fluorescence: rate and density-matrix regimes for plasma diagnostics *Plasma Sources Sci. Technol.* **29** 054001

[39] van Gessel A F H, van Grootel S C and Bruggeman P J 2013 *Plasma Sources Sci. Technol.* **22** 055010

[40] Bischel W K, Perry B E and Crosley D R 1982 Detection of fluorescence from O and N atoms induced by two-photon absorption *Appl. Opt.* **21** 1419–29

[41] Lucht R P, Salmon J T, King G B, Sweeney D W and Laurendeau N M 1983 Two-photon-excited fluorescence measurement of hydrogen atoms in flames *Opt. Lett.* **8** 365–7

[42] Gazeli K, Lombardi G, Aubert X, Duluard C Y, Prasanna S and Hassouni K 2021 Progresses on the use of two-photon absorption laser induced fluorescence (TALIF) diagnostics for measuring absolute atomic densities in plasmas and flames *Plasma* **4** 145–71

[43] Döbele H F, Mosbach T, Niemi K and Gathen V S D 2005 Laser-induced fluorescence measurements of absolute atomic densities: concepts and limitations *Plasma Sources Sci. Technol.* **14** S31–41

[44] Bischel W K, Perry B E and Crosley D R 1981 Two-photon laser-induced fluorescence in oxygen and nitrogen atoms *Chem. Phys. Lett.* **82** 85–88

[45] Niemi K, Gathen V S D and Döbele H F 2001 Absolute calibration of atomic density measurements by laser-induced fluorescence spectroscopy with two-photon excitation *J. Phys. D: Appl. Phys.* **34** 2330–5

[46] Preppernau B L, Pearce K, Tserepi A, Wurzberg E and Miller T A 1995 Angular momentum state mixing and quenching of $n = 3$ atomic hydrogen fluorescence *Chem. Phys.* **196** 371–81

[47] Horiguchi H, Chang R S F and Setser D W 1981 Radiative lifetimes and two-body collisional deactivation rate constants in Ar for Xe(5p56p), Xe(5p56p), and Xe(5p57p) states *J. Chem. Phys.* **75** 1207–18

[48] Chang R S F, Horiguchi H and Setser D W 1980 Radiative lifetimes and two-body collisional deactivation rate constants in argon for Kr(4p 55p) and Kr(4p 55p$'$) states *J. Chem. Phys.* **73** 778–90

[49] Drag C, Marmuse F and Blondel C 2021 Measurement of the two-photon excitation cross-section of the 6p'[3/2]2 and 6p'[1/2]0 levels of Xe I at the wavelengths 224.3 and 222.6 nm *Plasma Sources Sci. Technol.* **30** 075026

[50] Maitre P-A, Bieniek M S and Kechagiopoulos P N 2021 Modelling excited species and their role on kinetic pathways in the non-oxidative coupling of methane by dielectric barrier discharge *Chem. Eng. Sci.* **234** 116399

[51] Bieniek M S, Santos D F N, Almeida P G C and Benilov M S 2018 Bifurcations in the theory of current transfer to cathodes of DC discharges and observations of transitions between different modes *Phys. Plasmas* **25** 042307

[52] Wang Q, Economou D J and Donnelly V M 2006 Simulation of a direct current microplasma discharge in helium at atmospheric pressure *J. Appl. Phys.* **100** 023301
[53] Raizer Y P 1991 *Gas Discharge Physics* ed J E Allen (Berlin: Springer)
[54] Hagelaar G J M and Pitchford L C 2005 Solving the Boltzmann equation to obtain electron transport coefficients and rate coefficients for fluid models *Plasma Sources Sci. Technol.* **14** 722–33
[55] Bieniek M S, Walsh J L and Hasan M I 2021 Modeling the thermalization of electrons in conditions relevant to atmospheric pressure He-O_2 nanosecond pulsed discharges *Phys. Plasmas* **28** 063501
[56] Viehland database (available at: www.lxcat.net) (Accessed February 2022)
[57] Hagelaar G J M, de Hoog F J and Kroesen G M W 2000 *Phys. Rev.* E **62** 1452
[58] Fridman A 2008 *Plasma Chemistry* (Cambridge: Cambridge University Press) (https://doi.org/10.1002/chem.200800412)
[59] Bruggeman P and Schram D C 2010 On OH production in water containing atmospheric pressure plasmas *Plasma Sources Sci. Technol.* **19** 045025
[60] Murakami T, Niemi K, Gans T, O'Connell D and Graham W G 2012 Chemical kinetics and reactive species in atmospheric pressure helium–oxygen plasmas with humid-air impurities *Plasma Sources Sci. Technol.* **22** 015003
[61] Hasan M I and Bradley J W 2015 Computational study of the afterglow in single and sequential pulsing of an atmospheric-pressure plasma jet *Plasma Sources Sci. Technol.* **24** 055015
[62] SIGLO database (available at: www.lxcat.net) (Accessed February 2022)
[63] Breden D, Miki K and Raja L L 2012 Self-consistent two-dimensional modeling of cold atmospheric-pressure plasma jets/bullets *Plasma Sources Sci. Technol.* **21** 034011
[64] MORGAN database (available at: www.lxcat.net) (Accessed February 2022)
[65] Murakami T, Niemi K, Gans T, O'Connell D and Graham W G 2013 Interacting kinetics of neutral and ionic species in an atmospheric-pressure helium–oxygen plasma with humid air impurities *Plasma Sources Sci. Technol.* **22** 045010
[66] ITIKAWA database (available at: www.lxcat.net) (Accessed February 2022)